Article

Cell Reports

The Selective Autophagy Receptor p62 Forms a Flexible Filamentous Helical Scaffold

Graphical Abstract

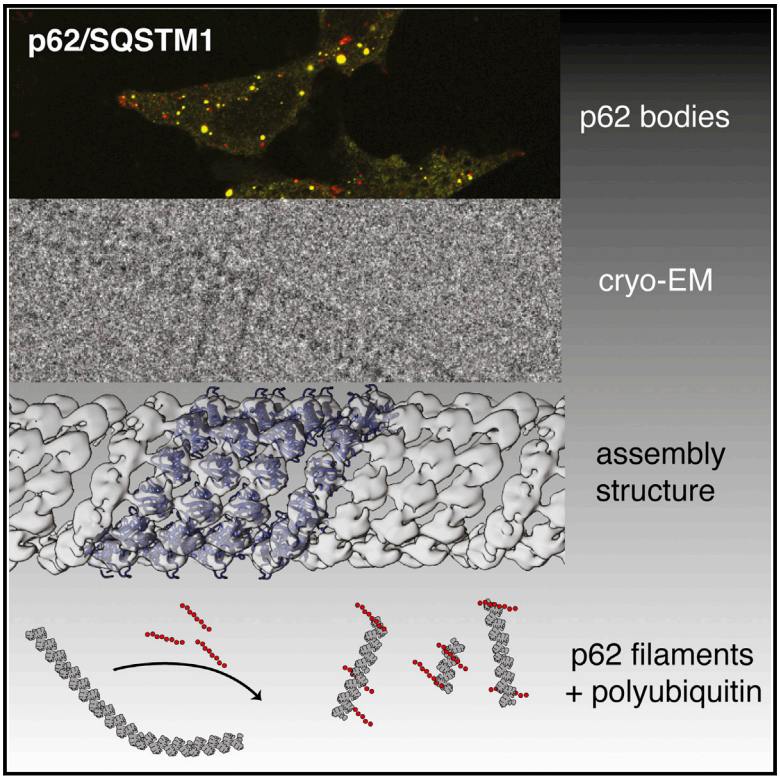

Authors

Rodolfo Ciuffa, Trond Lamark, ..., Terje Johansen, Carsten Sachse

Correspondence

carsten.sachse@embl.de

In Brief

The scaffold protein p62/SQSTM1 is involved in protein turnover and signaling and forms a punctate pattern in eukaryotic cells. Ciuffa et al. show that, based on the PB1 domain scaffold, p62 forms helical protein superstructures that are able to act as autophagy receptors by interacting with LC3 and polyubiquitin.

Highlights

- Autophagy receptor p62/SQSTM1 forms helical filaments based on a PB1 domain scaffold
- p62 polymers are stabilized by an electrostatic bridge C-terminal to the PB1 domain
- p62 filaments act as autophagy receptors as they interact with LC3 and polyubiquitin
- Polyubiquitin chains can regulate length of p62 helices by filament shortening

Ciuffa et al., 2015, Cell Reports *11*, 748–758
May 5, 2015
http://dx.doi.org/10.1016/j.celrep.2015.03.062

CellPress

OPEN ACCESS
CellPress

Cell Reports
Article

The Selective Autophagy Receptor p62 Forms a Flexible Filamentous Helical Scaffold

Rodolfo Ciuffa,[1] Trond Lamark,[2] Abul K. Tarafder,[1] Audrey Guesdon,[1] Sofia Rybina,[1] Wim J.H. Hagen,[1] Terje Johansen,[2] and Carsten Sachse[1,*]

[1]European Molecular Biology Laboratory, Structural and Computation Biology Unit, Meyerhofstrasse 1, 69117 Heidelberg, Germany
[2]Molecular Cancer Research Group, Institute of Medical Biology, University of Tromsø – The Arctic University of Norway, 9037 Tromsø, Norway
*Correspondence: carsten.sachse@embl.de
http://dx.doi.org/10.1016/j.celrep.2015.03.062

SUMMARY

The scaffold protein p62/SQSTM1 is involved in protein turnover and signaling and is commonly found in dense protein bodies in eukaryotic cells. In autophagy, p62 acts as a selective autophagy receptor that recognizes and shuttles ubiquitinated proteins to the autophagosome for degradation. The structural organization of p62 in cellular bodies and the interplay of these assemblies with ubiquitin and the autophagic marker LC3 remain to be elucidated. Here, we present a cryo-EM structural analysis of p62. Together with structures of assemblies from the PB1 domain, we show that p62 is organized in flexible polymers with the PB1 domain constituting a helical scaffold. Filamentous p62 is capable of binding LC3 and addition of long ubiquitin chains induces disassembly and shortening of filaments. These studies explain how p62 assemblies provide a large molecular scaffold for the nascent autophagosome and reveal how they can bind ubiquitinated cargo.

INTRODUCTION

Macroautophagy (hereafter referred to as autophagy) is one of the two major cellular degradative pathways. In autophagy, a membrane organelle termed the autophagosome forms in the cytoplasm and engulfs molecules and organelles fated for lysosomal degradation. To date, more than 35 proteins have been described to be involved in this process (Mizushima et al., 2011). Recently, it has become clear that this process can be highly selective, when the cargo is labeled and recruited to autophagosomes by autophagy receptors (Mizushima et al., 2011; Johansen and Lamark, 2011; Pankiv et al., 2007; Bjørkøy et al., 2005). P62/SQSTM1 (from here referred to as p62) has emerged as a polymeric, modular protein with critical roles in autophagy, protein aggregation, and cell signaling (Moscat and Diaz-Meco, 2009; Johansen and Lamark, 2011), and its misregulation has been implicated in neurodegenerative diseases, cancer, and inflammation (Moscat and Diaz-Meco, 2012).

Bioinformatic analysis reveals that p62 comprises three domains, two of which have been structurally characterized, as well as additional binding motifs. The N-terminal PB1 domain mediates homo- and hetero-dimerization (Lamark et al., 2003; Saio et al., 2009; Wilson et al., 2003). The Kelch-like ECH-associated protein 1 (KEAP1) binding motif (KIR) is involved in regulating the activation of the oxidative stress response transcription factor NRF2 (Jain et al., 2010; Lau et al., 2010; Komatsu et al., 2010). The LC3/ATG8 interacting region (LIR) associates with the autophagosomal marker LC3/ATG8 (Pankiv et al., 2007; Ichimura et al., 2008), and the C-terminal UBA domain binds ubiquitinated proteins (Long et al., 2010). Several lines of evidence demonstrate that p62 is implicated in the disposal of ubiquitinated cargoes, ranging in size from proteins and protein aggregates to organelles, in addition to viruses and bacteria (Johansen and Lamark, 2011). A receptor function has been proposed since p62 recognizes ubiquitinated proteins via its UBA domain, and the LIR sequence connects to the autophagosomal membrane via LC3. Consequently, p62 associates with misfolded proteins and protein aggregates into a sequestosome or so-called p62 bodies and provides a scaffold to nucleate autophagosome formation and subsequent degradation (Johansen and Lamark, 2011).

Previous studies have revealed that MBP- or GST-p62 fusions can form large aggregate structures in vitro (Wilson et al., 2003; Paine et al., 2005), and in p62 transfected cells protein-dense clusters or arrays have been observed by electron microscopy (EM) (Johansen and Lamark, 2011; Zatloukal et al., 2002; Stumptner et al., 2007). Biophysical characterization of p62 has shown that p62 aggregation over time is accompanied by an increase in β sheet content (Paine et al., 2005). In vivo studies indicate that the oligomeric state of p62 is required both for the association and sequestration of cargoes and for the delivery of p62 to the autophagosomes (Bjørkøy et al., 2005; Itakura and Mizushima, 2011; Ichimura et al., 2008). PB1-domain-mediated polymerization of p62 is also important for activation of the oxidative stress response regulating transcription factor NRF2 (Jain et al., 2010; Komatsu et al., 2010). How cellular levels of p62 affect protein aggregation in vivo has been subject to debate. First, immunohistochemical studies have identified p62 in many liver and neurodegenerative disease aggregates, such as Mallory bodies in alcohol hepatitis, Hyaline bodies in hepatocellular carcinoma,

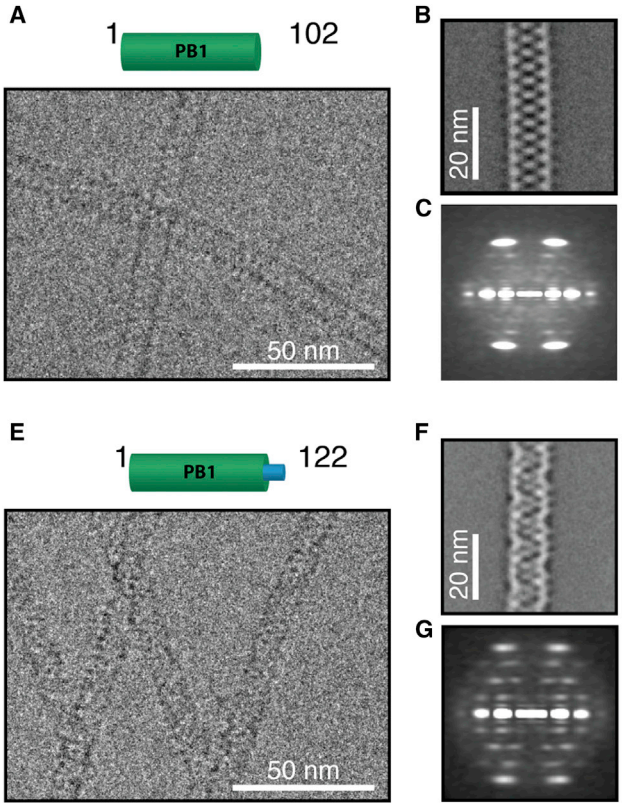

Figure 1. 3D Cryo-EM Structures of Helical PB1 and PB1 Assemblies

(A–D) Analysis of PB1 (1–102). Primary structure and electron cryo-micrographs of selected filaments (A) with a representative class average (B) and corresponding sum of the power spectra (C; highest resolution layer line at 1/38 $Å^{-1}$) and (D) 3D structure (σ = 1.7).

(E–H) Analysis of the tubular form of PB1 (1–120) type T. Primary structure and electron cryo-micrographs of selected PB1 triple helix (E) with a representative class average (F) and corresponding sum of the power spectra (G;highest resolution layer line at ~1/34 $Å^{-1}$) and 3D structure (H) (σ = 1.7; see also Figures S1 and S2).

Lewy bodies in Parkinson's disease and neurofibrillary tangles in Alzheimer's disease (Kuusisto et al., 2001; Zatloukal et al., 2002). Therefore, it has been proposed that the polymerization of p62 itself may be the source of some of these cytotoxic inclusions, playing a supporting role to stimulate their formation. Second, increased p62 levels caused by inactivation of autophagy promote the formation of ubiquitinated protein aggregates (Komatsu et al., 2007; Moscat and Diaz-Meco, 2009; Johansen and Lamark, 2011). Third, also the genetic inactivation of p62 can exacerbate the aggregation process (Ramesh Babu et al., 2008). Taken together, these data suggest that polymerization and regulation of the oligomeric state of p62 is key to understanding its physiological role in autophagy, cell signaling, and in aberrant protein aggregation processes that lead to neurodegeneration, liver, and muscle diseases.

Despite the importance of p62 in protein turnover and signaling, to date, it is not clear how p62 is structurally organized in oligomers or polymers as no molecular structure of p62 assemblies has been reported. Moreover, how a single protein, p62, conducts the receptor and scaffold function remains unknown. Using electron cryo-microscopy (cryo-EM), we show that p62 is organized in a three-dimensional helical assembly, whose scaffold is formed by the PB1 domain. The assembly structure interacts with cellular binding partners LC3 and ubiquitin via the LIR motif and UBA domain that make up an accessible C-terminal p62 region in the filaments. Based on our experiments, we propose a model of how p62 helical assemblies can act as a large molecular scaffold to achieve membrane elongation and how it can bind ubiquitinated cargo.

RESULTS

The PB1 Domain Assembles to Form Flexible Helical Polymers

We set out to purify and structurally characterize the autophagy receptor p62 by cryo-EM. First, we focused on the PB1 domain, which has been shown to be responsible for polymerization of p62 (Wilson et al., 2003; Lamark et al., 2003; Johansen and Lamark, 2011; Saio et al., 2009) and purified two PB1 domain constructs PB1 (1–102) and PB1 (1–122) including an additional 20 residues (Wilson et al., 2003; Pankiv et al., 2007). We found that the two PB1 domain samples gave rise to flexible but structurally ordered polymers (Figures 1A and 1E) that appeared suitable for image analysis and 3D image reconstruction. When we prepared PB1 (1–122) samples using ammonium sulfate precipitation, they gave rise to tubular structures (type T), whereas in the absence of the precipitation step the assemblies had a filamentous appearance (type F) (Figure S1A). Classification analysis of segmented PB1 (1–102), PB1 (1–122) type F and type T (Figures 1B and 1F; Figure S1B) showed long, 15-nm-wide helically wound ribbons with an average helical pitch of 3.8 ± 0.1, 13.6 ± 0.2, and 15.6 ± 0.7 nm, respectively (Figures S1E, S1F, and S2A). Although Fourier analysis of segments from PB1 (1–102) and both type T and F PB1 (1–122) demonstrated the presence of layer lines indicative of helical order (Figures 1C, 1G, and S1C), none of the power spectra of the classes revealed helical order beyond ~1/34 Å. Using electron tomography, we determined that type F PB1 (1–122) filaments possess a left-handed helical twist (Figure S1G). Given the close relationship of the samples, we infer that the left hand is preserved in the two PB1 samples and assembly types.

PB1 Polymers Share a Common Core Strand of Helical PB1 Domains

Next, we determined the cryo-EM structures of PB1 (1–102), PB1 (1–122) type T and type F assemblies using a previously described single-particle helical image reconstruction method (Desfosses et al., 2014) (processing details are in Table S1).

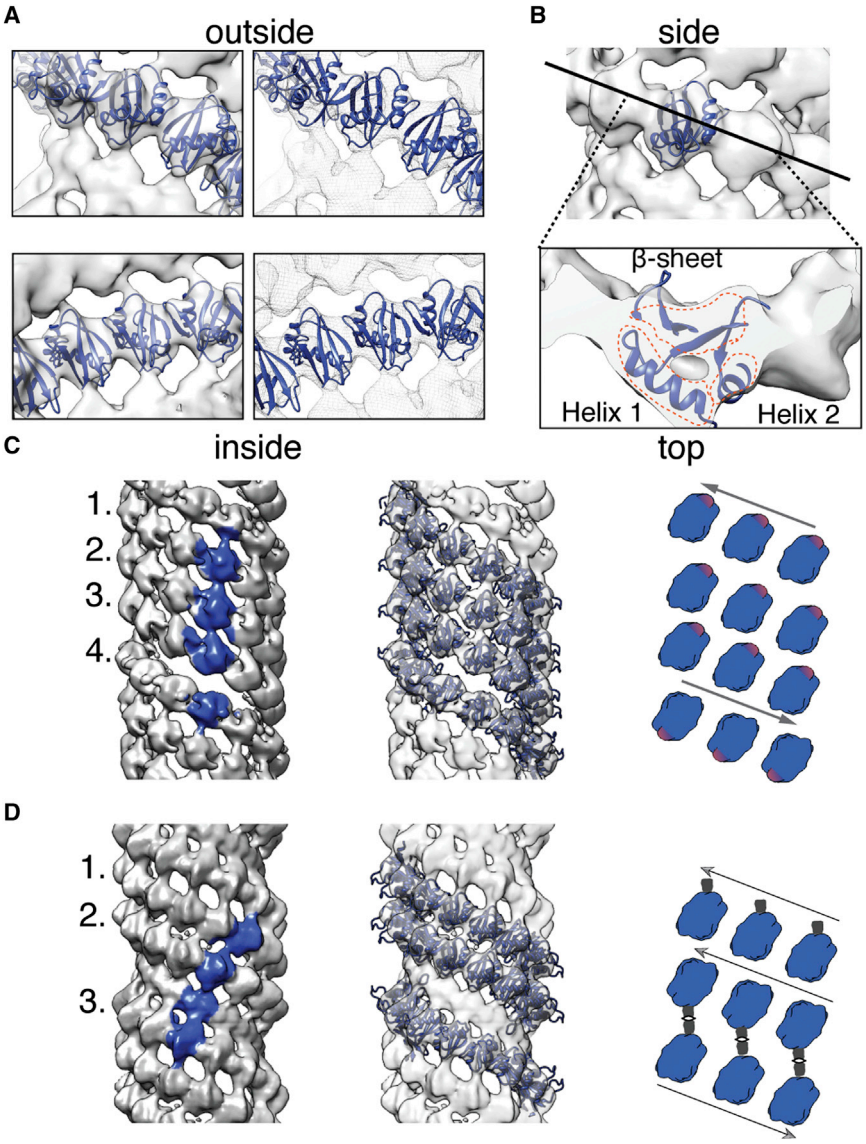

Figure 2. Fit and Principal Architecture of PB1 Polymers

Rigid-body fit of the homologous human PB1 domain into the cryo-EM PB1 (1–102) and PB1 (1–122) type T structure.

(A) Surface and mesh EM density presentation of type T structure (left and right) from the outside and inside of the helix (top and bottom).

(B) A section through the PB1 volume (the plane indicated by the black bar) reveals a density compatible with the fold of the PB1 domain.

(C and D) Cryo-EM structures of PB1 (1–102) (C) and PB1 (1–122) type T (D). Left: Surface-rendered side view with highlighted asymmetric unit PB1 domain (blue). Center: Rigid body fit of the PB1 domain (blue) and (right) cartoon illustrating the organization of the subunits inside the polymers (see also Figure S2).

We resolved the PB1 (1–102) and PB1 (1–122) type T structure (Figures 1D and 1H) at ~10.9 Å and 10.3 Å resolution, respectively, as estimated from the Fourier shell correlation (Figure S2F). The PB1 (1–102) EM density reveals a four-stranded helical wrung of PB1 domains. Using scanning transmission electron microscopy (STEM), we determined the mass-per-length of PB1 (1–102) polymers as 37.0 kDa/nm (Figure S2B). Taking into account pitch measurements and symmetry refinement (Figures S2A and S2C), the analysis reveals that the PB1 helix is constituted of 11.7 units per turn, while four PB1 domains make up the helical unit of the assembly. The smooth cryo-EM map of PB1 (1–122) type F (Figure S1D) reveals that two PB1 strands run in opposite directions and are joined by a connecting density. The helical asymmetric unit comprises two PB1 subunits that are related by a local 2-fold axis running perpendicularly to the helix axis, which relates the opposite PB1 subunits by 180° rotation. The double strand is also present in the higher resolution PB1 type T map but is complemented by a third PB1 strand that seals the filament to form a closed structure giving rise to a slightly lower pitch of 13.5 nm. Using the mass-per-length values of 27.7 and 40.7 kDa/nm determined by STEM followed by symmetry refinement (Figures S1H and S1I), we found that a total of ~15.7 and ~13.5 subunits make up a single helical turn in the type F and T PB1 (1–122) assemblies (Figures S1J and S1K), respectively. The obtained values are close to the broad ranges of a modeled PB1 helical polymer (Figure S2G) based on the NMR dimer structure (Saio et al., 2010). Hence, while both PB1 (1–122) domain structures share a double helix of PB1 domains, the PB1 type T accommodates a third additional strand of PB1 domains that confers polarity to the helix. Given the observed structural diversity of helical PB1 domain scaffolds, it is important to consider that the precise arrangements of the observed PB1 assemblies are specific to the expressed PB1 domain length. The determined structures of all constructs share the basic helical scaffold of the PB1 domain.

To further interpret the EM densities, the PB1 (1–102) and PB1 (1–122) type T maps were manually fitted with the structure of the PB1 domain of the rat homolog (PDB code 2kkc). In both maps, the size of the globular density matches the PB1 domain dimension (Figure 2). At a lower isosurface threshold of the PB1 type T map, the outline of the globular density matches the overall PB1 fold composed of two α helices packed against a β sheet and provides good guidance for the fitting procedure (Figure 2B). The fitted PB1 molecules preserve the dimer interface of the homologous PB1 structures (Wilson et al., 2003; Saio et al., 2010) (Figures 2C and 2D).

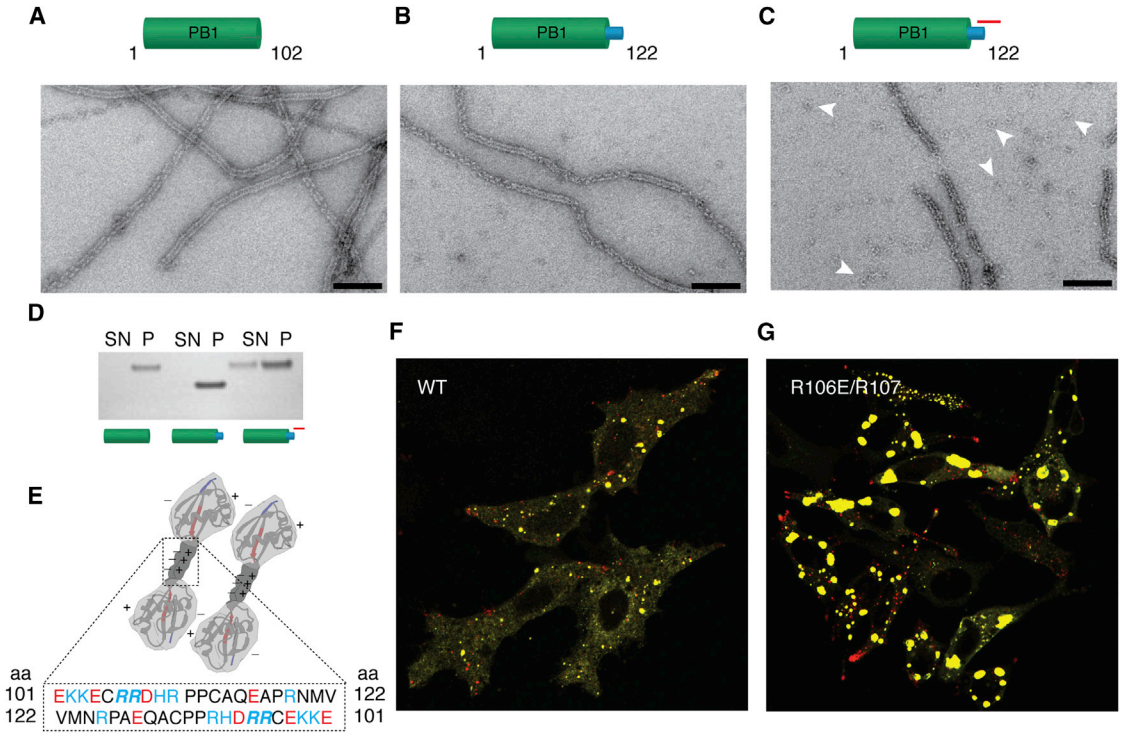

Figure 3. PB1 Helix Is Stabilized by an Electrostatic PB1 Bridge

(A–C) Mutation analysis and comparison of different PB1 domain constructs using negative stain electron micrographs and sedimentation analysis: PB1 (1–102) (A), PB1 (1–122) (B), and PB1 (R106E/R107E; C; scale bars, 100 nm).

(C) Introduction of negative charges (R106E/R107E) into the PB1 (1–122) construct gives rise to few disrupted filaments and many oligomers of open and closed ring shapes (white arrows).

(D) Charge mutations shift the sedimentation equilibrium from the pellet to supernatant.

(E) Cartoon illustrating the interaction model of the PB1 domain with dihedral symmetry axis.

(F and G) Overexpression of the charge-reversal mutant mCherry-EYFP-p62 in human HeLa cells upon siRNA knockdown of endogenous p62 results in the formation of larger protein aggregates than wild-type p62. Red punctae indicate that the charge-reversal is degraded by autophagy similar to wild-type p62 (see also Figures S4 and S6).

The PB1 Strands Are Stabilized by a C-Terminal Extension

The superposition of the fitted PB1 structure with the cryo-EM map suggests that the central densities between the antiparallel strands correspond to additional C-terminal 22 residues of our construct where no previous structural information is currently available. In the PB1 (1–122) type T map, we found that the third strand projects additional density of the 22 C-terminal residues to the lumen of the tubular assembly. Electron micrographs of the PB1 (1–102) and PB1 (1–122) revealed tubular and filamentous assemblies (Figures 3A and 3B). Sedimentation analysis of PB1 (1–102) and PB1 (1–122) showed that both purified constructs pellet almost completely (Figure 3D). Based on the observation that the 100–122 region is rich in basic and acidic residues, we designed a charge-reversal mutant (R106E/R107E) (Figures 3C–3E and 3G). Both the visualization by electron microscopy of the structure-based mutant and sedimentation assays with the structure-based mutant confirmed the stabilizing role of the C-terminal extension (103–122) of the PB1 domain. In the EM images, we observed oligomers of open and closed ring shapes and few disrupted filaments with the mutant when compared with compact filamentous wild-type PB1 (1–102) and (1–122) polymers (Figure 3C).

Overexpression of full-length mCherry-EYFP-p62 containing the charge-reversal mutant in human HeLa cells led to the formation of larger protein aggregates than wild-type p62 in the presence of p62 knockdown small interfering RNA (siRNA) (Figures 3F and 3G; Figure S3). In the case of R106E/R107E mutant, almost 50% of the cells scored (29 of 61) had aggregates with a diameter above 5 μm, while only 14% (6 of 43) of the cells overexpressing wild-type GFP-p62 had such large aggregates. Moreover, we analyzed a pH-sensitive mCherry-EYFP R106E/R107E to monitor the ability of the mutant to undergo autophagy. The mutant showed enhanced aggregation properties when compared with wild-type mCherry-EYFP p62 but can still undergo degradation by autophagy. In addition, we generated a stable cell line expressing the R106E/R107E p62 mutant that exhibits enhanced aggregation behavior when compared with wild-type p62 (Figure S4A). The fraction of cells with p62 punctae larger than 1 μm increased from 23% to 50% determined from 478 and 624 cells expressing wild-type and mutant p62 (Figure S4C). When autophagic degradation is blocked by addition

of bafilomycin A1, buildup of R106E/R107E mutant aggregates was similar to wild-type p62 suggesting an equal capability of autophagy sequestration (Figure S4B). Hence, it is the cellular aggregation and not the degradation that is affected by the charge-reversal mutant. In conclusion, the perturbation of ordered polymerization in vitro is in agreement with enhanced punctae formation in vivo as the charge-reversal mutant still forms relatively large oligomers of open and closed ring shapes when compared with the symmetric and compact PB1 domain helices. The pseudo-atomic model derived from the PB1 type T map reveals that the additional 22 C-terminal residues of the PB1 construct make up an electrostatic PB1 bridge stabilizing the PB1 assembly alone but also in the in vivo context of full-length p62.

PB1 Constitutes the Helical Scaffold of p62 Filaments

Next, we purified and imaged PB1 including the ZZ domain (1–167; from now on referred to simply as PB1-ZZ) using cryo-EM (Figure 4A). The PB1-ZZ assemblies matched the closed tubular arrangement of PB1 type T with a comparable width of 15 nm. Class averages revealed that the majority of the PB1-ZZ sample, approximately 80%, gave rise to featureless tubules, while only 20% showed detailed structural features (Figure 4B) of an average pitch of 12.2 ± 0.6 nm (Figure 4C). The apparent dihedral symmetry of the PB1-ZZ class averages suggests that the PB1-ZZ filament is also organized in a double helix similar to PB1 (1–122) type F with additional densities to accommodate the ZZ domain.

Finally, we investigated the polymer structure of the full-length p62 that shows ribbon-like assemblies (Figure 4D), although it is more irregular and forms significantly shorter filaments (40.7 ± 27.6 nm) than the PB1 domain structures (>500 nm). Approximately 38% of the class averages showed low-resolution helical features whereas 62% are elongated but possess tubular and more irregular features (Figure 4E). The well-defined p62 helices with a recognizable pitch of 14.8 ± 1.1 nm (Figures 4F and 4G) have an asymmetric spring-like appearance with diameters ranging from 150 to 160 Å (Figure 4H). The density distribution of the class averages indicated that no dihedral symmetry is present in the assembly suggesting that only a single PB1 strand forms the scaffold. The re-projection of a single PB1 strand matches the smaller radius in the p62 class averages (Figure 4I) with the remaining part of the larger radius corresponding to the ZZ domain and the C-terminal p62 region (Figure 4J). This interpretation is consistent with the fact that about one-quarter of the protein sequence constitutes the PB1 domain, and the size of the remaining density matches approximately the size of the remaining C-terminal sequence of p62. Predicted structural disorder of residues between the ZZ and UBA domain may contribute to the observed heterogeneity and flexibility and thus rendering it impossible to determine the helical parameters and a unique 3D structure.

The three determined cryo-EM structures from the PB1 domains and the cryo-EM images from PB1-ZZ and the full-length p62 assembly reveal a common motif of a core strand of PB1 domains. The PB1 domain strand is followed by the ZZ domain, and the remaining part makes up the solvent-accessible C terminus of the full-length helical assembly. These in vitro results substantiate the hypothesis that PB1 forms the helical template of p62, and they are in agreement with previous in vivo studies (Pankiv et al., 2007; Bjørkøy et al., 2005), which have shown that central deletions of p62 were still functional in forming p62 bodies in the cell.

Octa-Ubiquitin, but Not LC3, Binding to p62 Results in Filament Shortening

The two main autophagic interaction partners of p62 are ubiquitin in the form of ubiquitinated cargo and LC3/Atg8 that is linked to the autophagosomal membrane (Pankiv et al., 2007; Bjørkøy et al., 2005). Since it has been shown that LC3 and ubiquitin are interacting with p62, we tested the ability of these binding partners to interact with p62 filamentous assemblies. In order to address this question, we performed a co-sedimentation assay of p62 in the presence of increasing concentrations of LC3. The results of the co-sedimentation assay showed that molar excess of LC3 binds filamentous p62 but does not alter the sedimentation behavior of p62 (Figure 5A). When K63-linked octa-ubiquitin was added in excess to filamentous p62, it induced entire disassembly and disappearance of polymers (Figures 5B and 5C). At lower concentrations of octa-ubiquitin, p62 polymers appeared shortened to helical stubs when observed by electron microscopy (Figure 5D). Importantly, the same molar ratios of octa-ubiquitin had no effect on p62 ΔUBA filament length (Figure S5A). By contrast, when visualizing mono- and di-ubiquitin incubated with p62, no shortening of the filaments was observed (Figures S5B and S5C). Although we cannot exclude minor effects of solubilization through mono-ubiquitin or di-ubiquitin, we find that longer K63-linked octa-ubiquitin chains efficiently disassemble p62 filaments through UBA domain interactions.

Consistent with these in vitro observations, we found that ubiquitin overexpression in vivo inhibited p62 body formation in human RPE1 cells treated with puromycin to induce protein aggregation (Figure 5F). Quantification showed that high levels of ubiquitin correspond to a significant decrease in punctae formation (Student's t test $p < 0.01$ for high myc-Ub versus low myc-Ub and high myc-Ub versus myc-Ub negative) (Figure S6). These results indicate that the described self-interactions of UBA domains and ubiquitin-UBA interaction (Ciani et al., 2003; Long et al., 2010; Ichimura et al., 2008; Saio et al., 2009) may take place at the accessible C terminus and at the ends of the p62 helix to destabilize the polymeric assembly. Taken together, the p62 helices are recognized and bound by LC3, while K63-linked octa-ubiquitin binding is able to induce the disassembly of the p62 helix. The presented biochemical data support the structural interpretation that the LIR motif and UBA domain are accessible in the p62 helix. Our finding suggests that binding partners such as ubiquitin may be critical in regulating the length of p62 polymers, and that increased cargo binding switches the protein from a polymeric to a different assembly state.

DISCUSSION

We have found that p62 forms flexible helical polymers in vitro of up to 100 s of nanometers or 0.1 μm in length and approximately

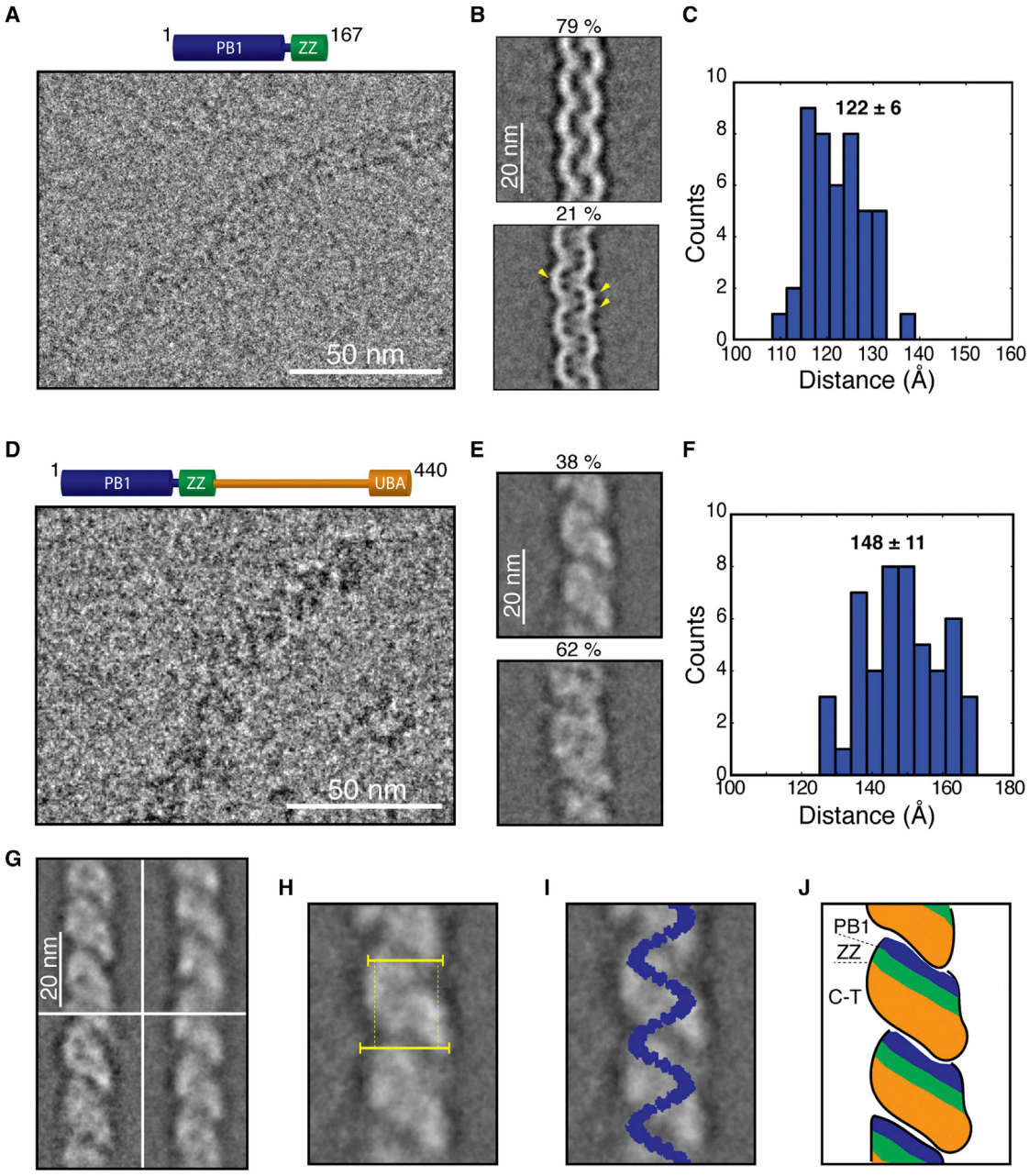

Figure 4. Cryo-EM Images of PB1-ZZ and p62 Helix

(A) Primary structure and electron cryo-micrograph of PB1-ZZ assembly.

(B) 79% of the class averages show featureless tubular structures, while 21% give rise to assemblies with defined features details (arrows).

(C) Histogram of pitch distribution of 12.2 ± 0.6 nm (mean ± SD) measured from class averages.

(D) Primary structure (top) and electron micrographs (bottom) of full-length p62 embedded in vitreous ice.

(E) Representative class averages illustrate the heterogeneity of the sample. A total of 38% have recognizable pitch features, while 62% correspond to tubular or more irregular assemblies.

(F) Pitch distribution of full-length p62 determined at 14.8 ± 1.1 nm.

(G) Four representative classes with defined pitch features have a spring-like appearance.

(H) A representative class average with highlighted width difference in yellow.

(I) Superposition of thresholded reprojection of a single PB1 helical strand (in blue).

(J) Cartoon illustrating the putative arrangement of the p62 domains in the polymer and highlighting the presence of a PB1 scaffold (blue), the ZZ domain (green), and a C-terminal stretch (orange) including the unstructured region and the UBA domain.

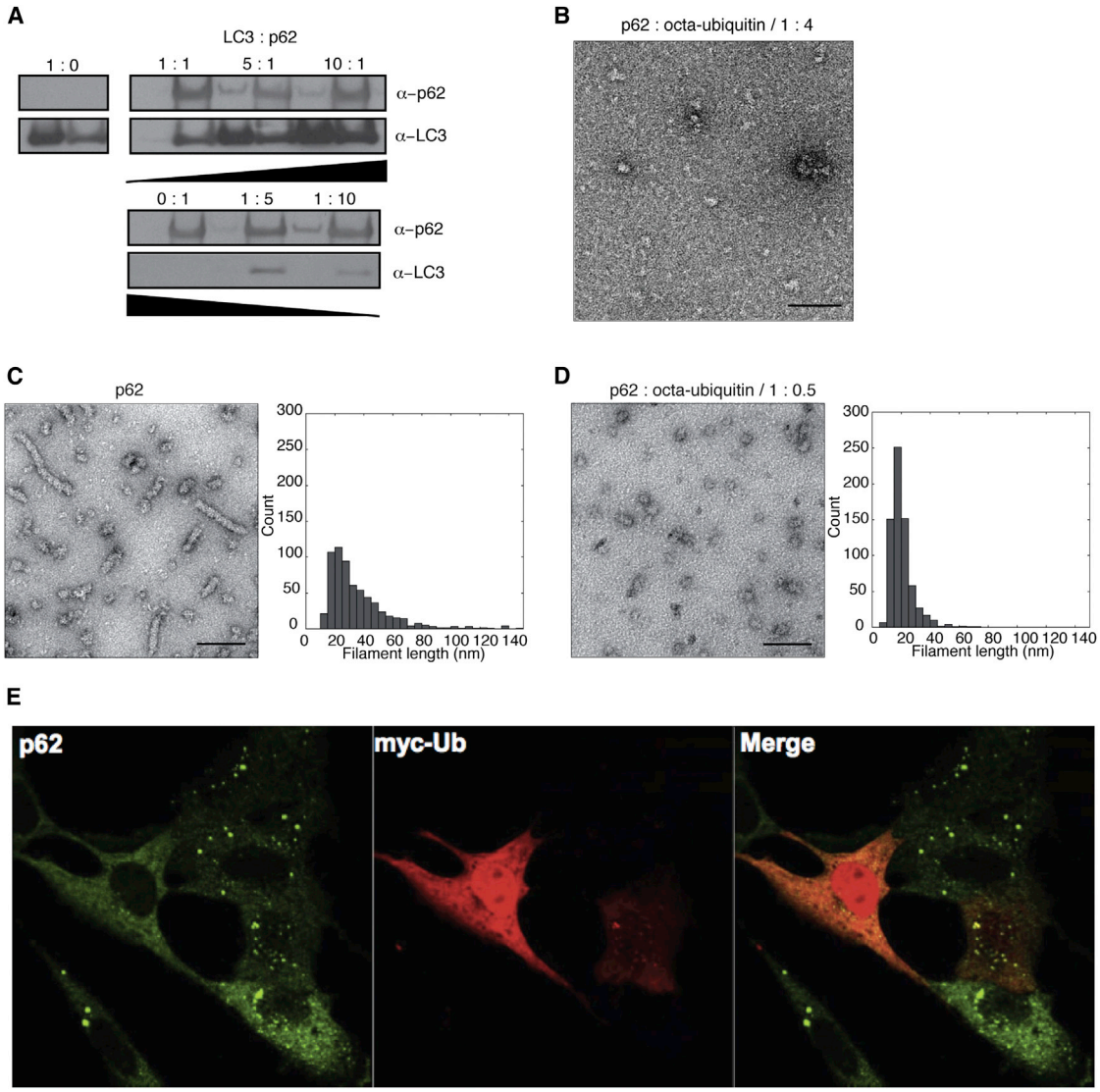

Figure 5. Ubiquitin and LC3 Interaction with the p62 Helix

(A) Co-sedimentation assay of p62/LC3 (increasing amount of LC3) confirms that LC3 interacts with filamentous p62.

(B) Electron micrograph reveals that the addition of excess K63-linked octa-ubiquitin (molar ratio 1:4) to filamentous p62 induces disassembly.

(C and D) Electron micrographs and length histogram of p62 alone (C) and p62 incubated with octa-ubiquitin at intermediate molar ratio (1:0.5; D) confirm that ubiquitin interaction induces shortening of p62 helices (scale bars, 100 nm).

(E) High levels of ubiquitin decrease the extent of p62 body formation. Overexpression of myc-ubiquitin (red) by transient transfection inhibits formation of p62 bodies (green) following induction of protein aggregation by puromycin treatment of human RPE-1 cells (see also Figures S4 and S6).

15 nm in width. We further found that they constitute flexible polymers indicated by significant curvature and pitch variation in contrast to rigid viral assemblies (Sachse et al., 2007), a fact that currently impedes the determination of high-resolution structures. The presented EM data are in agreement with light microscopy observations of punctate p62 bodies (Pankiv et al., 2007; Zatloukal et al., 2002). Nuclear and cellular inclusions of p62 of about 0.1 and 2 μm in diameter were identified (Bjørkøy et al., 2005; Johansen and Lamark, 2011; Kishi-Itakura et al., 2014). EM sections of cells transfected with p62 exhibit clustered arrays of 10- to 15-nm-wide filaments (Stumptner et al., 2007) emphasizing the physiological relevance of the p62 helices resolved in this study. Given the compact nature of helical p62 assemblies demonstrated in the present study, p62 filaments could make up the protein bulk of p62 bodies. At this point, however, it is only the work of Stumptner et al. (2007) suggesting that p62 filaments exist in cells. This cryo-EM study reveals that p62 forms a helical assembly built from a core PB1 strand scaffold with the C-terminal part of p62 attached to host binding sites with interacting partners of p62 that have been described (Bjørkøy et al., 2005; Pankiv et al., 2007; Jain et al., 2010), in particular, LC3, KEAP1, and ubiquitin.

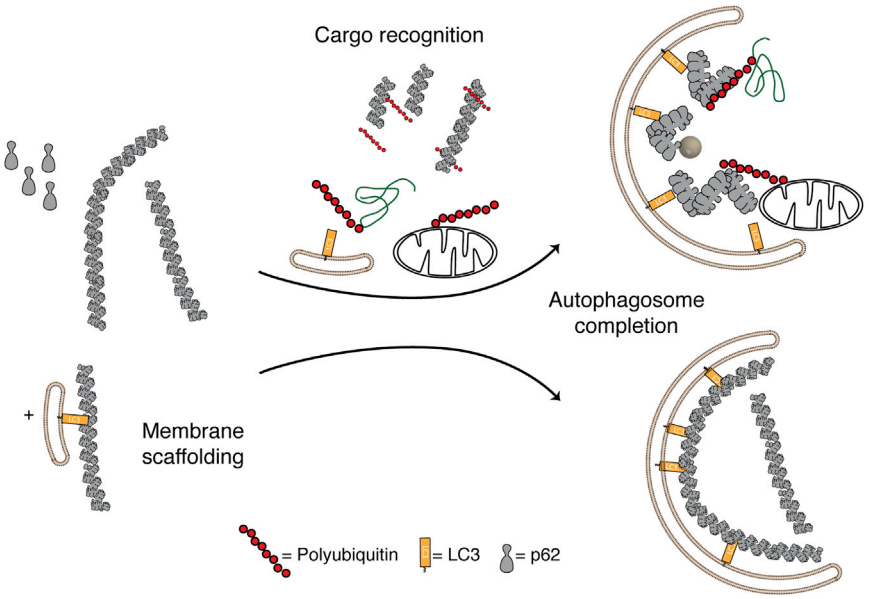

Figure 6. Scaffold and Receptor Function of p62

Cartoon model of scaffolding and receptor function of the p62 helix. Helical filaments serve as large molecular templates to nucleate the growing autophagosomal membrane mediated by the LC3 interactions. Upon recognition of ubiquitinated cargo, such as protein aggregates and organelles, membrane-bound and soluble p62 form shorter filaments that could also be crosslinked with ubiquitin chains. Thus, membrane-bound p62 filaments, as part of larger p62 bodies can mediate exclusive sequestration of cargo into the forming autophagosome via multiple LC3 interactions.

p62-PB1 belongs to a sub-family of PB1 domains that contain oppositely charged patches responsible for forming oligomers. The variety of observed configurations of core strands of helical PB1 domains potentially reveals an additional level of complexity in possible assembly configurations of p62 and related PB1 domain assemblies. The finding that the PB1 domain constitutes the template of a helical assembly raises the question whether other PB1 domain containing proteins can form similar structures as has been shown with the PB1-like domain protein Par-3 (Zhang et al., 2013). Some of the interactions p62 participates in are mediated by the PB1 domain and can therefore potentially interfere with its polymerization and may limit further oligomerization. For example, NBR1 or the atypical protein kinase C, which contain PB1 domains incapable of forming polymers, may form heterooligomers that cap p62 via the PB1 domain to prevent the elongation to a p62 helix assembly, or alternative assembly types could form. Besides its function as an autophagy scaffold and receptor, p62 plays an important role in several signaling pathways and in the transcriptional activation by NFκB and NRF2 (Johansen and Lamark, 2011; Moscat and Diaz-Meco, 2012). A question that is raised by our studies is whether p62 is required to be in a monomeric or oligomeric state to act in these cascades. For activation of NRF2, it was already demonstrated that PB1-mediated polymerization is required (Jain et al., 2010; Komatsu et al., 2010), whereas for NFκB it has not yet been determined. The binding between different types of PB1 domain proteins may add new layers of regulation to the supramolecular organization of the signaling molecule p62.

We have shown that an additional stretch of residues C-terminal to the PB1 domain forms an electrostatic PB1 bridge that stabilizes the helical polymer. Disturbing the electrostatic bridge leads to formation of ring oligomers in vitro and in full-length p62 in cells reveals that it affects the aggregation properties of p62 while still retaining the ability to be degraded by autophagy. Interestingly, a ubiquitination site has been identified at K13 in spatial proximity to the electrostatic bridge (Kim et al., 2011), suggesting that, under certain circumstances, depolymerization of the helix may also be induced. Furthermore, posttranslational modifications of residues that are located in the PB1 helix interface (Kim et al., 2011), including PKA-mediated phosphorylation of S24 (Christian et al., 2014), and modifications that affect ubiquitin binding affinity such as phosphorylation of S403 (Matsumoto et al., 2011) will also affect the polymeric assembly state. Our 2D class averages of full-length p62 suggest that, while the PB1 domain forms the stable and folded core of the helical scaffold, the C-terminal part of the protein forms a solvent-accessible stretch. This architecture suggests a molecular mechanism by which p62 confines signaling interactions to defined cellular loci.

In addition, we demonstrate that K63-linked octa-ubiquitin chains can disassemble the p62 helix. Octa-ubiquitin chains induce efficient disassembly of polymeric p62 in contrast to mono or di-ubiquitins. Consequently, poly-ubiquitin chains and other p62 binding partners may have the ability to regulate the equilibrium between polymeric and oligomeric forms of p62 thereby preventing excessive aggregation (Figures 5B–5E). The specific mechanism by which ubiquitin depolymerizes p62 is not clear. In vitro studies of isolated UBA domains and ubiquitin indicate the destabilization of inter-UBA interactions upon addition of ubiquitin (Isogai et al., 2011). Therefore, ubiquitin may act by disrupting interaction surfaces involving the UBA domain in the helix critical for the helical assembly stability. In the absence of ubiquitin, specific intermolecular interactions of the UBA domain may contribute to p62 stability. This does not seem to be the case with the LIR domain as LC3 binding to p62 filaments does not cause disassembly. Interestingly, mutations in the UBA domain of p62 are linked to defects in osteoclastogenesis (Leach et al., 2006). Therefore, inadequate assembly length regulation mediated by ubiquitin may contribute to the aberrant processes described for Paget's disease of bone, as mutants are known to affect ubiquitin binding capacity.

Based on these data, we discuss a putative model that describes how p62 performs a key role in the scaffolding of the autophagosomal membrane and cargo recognition (Figure 6). We propose that p62 bodies are made up of organized helices

whose assembly and disassembly is regulated by a series of switches. Once p62 bodies interact with LC3-bound membrane, p62 helices are capable of forming the template for membrane elongation due to the many available LIR domains in the polymer. This interpretation is consistent with observations that p62 bodies were identified in structures free of membranes, i.e., sequestosomes, but also in the form of membrane-enwrapped p62 bodies (Bjørkøy et al., 2005). Biochemical studies in yeast have demonstrated that multiple LIR motifs or binding sites of Atg8 in the autophagy receptor Atg19 ensure the tight and exclusive enclosure of cargo (Sawa-Makarska et al., 2014). The unique ability of p62, however, to polymerize into large elongated assemblies may have the advantage that a series of p62's LIR motifs can efficiently bind to the membrane and enclose very large biological structures up to micrometer size such as protein aggregates and organelles (Johansen and Lamark, 2011). Our data support the idea that, after poly-ubiquitinated cargo is recognized by p62, this causes the formation of shorter and less compact helical filaments than those formed by p62 alone (Figure 6). At the current state of research, it is also possible to envision that at low concentrations poly-ubiquitin chains actively crosslink p62 filaments (Morimoto et al., 2015), whereas at molar excess poly-ubiquitin chains disassemble p62 filaments. Moreover, membrane-enwrapped p62 bodies can also enter the autophagosomal pathway without enclosing additional cytoplasmic material to be degraded (Bjørkøy et al., 2005). Thus, p62 bodies will have a cytoprotective function to target misfolded cytotoxic proteins for degradation, as p62 sequesters them and prevents their interference with basic cellular functions. Although p62 bodies can have a beneficial effect on sequestration of potentially cytotoxic material, it is clear that an intricate balance between soluble p62 and membrane-free and membrane-enwrapped p62 bodies is required to avoid excessive buildup of p62 aggregates in the cell in order to maintain cell homeostasis. The helical assemblies presented here reveal a large molecular scaffold with several critical switches that can modulate the filamentous assembly and therefore p62 receptor function in protein degradation and aggregation.

EXPERIMENTAL PROCEDURES

Protein Cloning, Expression, and Purification

MBP-p62 and MBP-PB1 plasmids were a gift of Roger Williams (MRC-LMB). All mutants (excluding p62Δ202-325), including all PB1 domain mutants of HA-p62 constructs, were generated using the site-directed mutagenesis kit (Stratagene) following the standard protocol. Maltose Binding Protein (MBP)-PB1 (1–102), MBP-PB1 (1–122), MBP-PB1-ZZ, MBP-p62 ΔUBA, and MPB-p62 fusion proteins were expressed in BL21 *Escherichia coli* in lysogeny broth (LB) medium. For MBP-PB1-ZZ, 1 mM $ZnCl_2$ was added to the expression medium. Cells were grown at 37°C until optical density (OD) exceeded 0.6, when the temperature was lowered to 20°C (24°C in the case of PB1 and PB1 mutants), and subsequently expression was induced at OD of 0.8 for 3.5 hr with 0.1 mM (0.05 mM in the case of p62) isopropyl β-D-1-thiogalactopyranoside (IPTG). Cells were lysed either by sonication, mechanical disruption, or by chemical lysis (Pierce B-PER Bacterial Protein Extraction Reagent). Subsequently, lysates were cleared using centrifugation for 25 min at 48,000 × *g* and applied on an affinity column with 2 ml suspension of amylose beads per gram of cell pellet and incubated for 1.5 hr at 4°C on a circular rotor. Fractions of MBP-p62 or MBP-p62 mutants were eluted with 10 mM maltose and loaded on a pre-equilibrated Superose 6 gel filtration column to remove low molecular weight impurities. The void volume was collected and cleaved overnight with His-tagged Tobacco Etch Virus (TEV) protease, and the cleaved protein was further separated from the tag using ammonium sulfate precipitation. After cleavage the protein contained an N-terminal linker of three residues (GSH). Prior to visualization in the electron microscope, the sample was dialysed against 50 mM Tris (pH 7.5), 50 mM NaCl (100 mM NaCl for PB1), 4 mM DTT. For purification of MBP-PB1, MBP-PB1-ZZ, or MBP-PB1 mutants, the affinity-purified protein was cleaved with His-TEV protease and separated from the tag using centrifugation for 1 hr at 48,000 × *g* or dialysis in a membrane with a MWCO of 100 kDa. If required, residual tag was removed by pelleting the protein through a 30% or a 60% glycerol cushion. The bottom fraction was collected and dialysed against 50 mM Tris (pH 7.5), 100 mM NaCl, DTT 4 mM. Subsequently, PB1, PB1-ZZ, and p62 samples were concentrated to 0.1–0.5 mg/ml.

STEM

Mass-per-length (MPL) measurement data were acquired at the Brookhaven National Laboratory according to previously described preparation and image acquisition conditions (Wall and Simon, 2001). Data were analyzed by using the computer program PCMASS29 with the 15-nm rod mask. In the PB1 (1–122) sample, we separated type F and type T helices visually into two populations before average mass determination. The MPL measurements of each micrograph were scaled to the expected MPL distribution of TMV as described (Diaz-Avalos et al., 2005).

Electron Microscopy

A total of 3.5 μl of PB1, PB1-ZZ, and p62 sample were applied to glow-discharged C-flat 1.2/1.3 and 200 mesh Quantifoil multi-A grids and plunge-frozen in a reservoir of liquid ethane using a custom-made cryo-plunger (PB1 [1–102], PB1 [1–122], PB1-ZZ) or an FEI Vitrobot (p62). Frozen grids were transferred to the FEI Titan Krios loading cassette for EM observation. Vitrified samples of PB1 type T/F, p62, and PB1-ZZ were imaged using a FEI Titan Krios at 120, 200, and 300 kV at a nominal magnification of 60,000 and 28,000. Micrographs were taken at an underfocus between 1.6 and 3.5 μm onto a Gatan US4000 4k × 4k CCD camera (PB1 type T/F, p62) or on a direct electron detector FEI Falcon II (PB1 [1–102], PB1-ZZ). We estimated the dose deposited on PB1 (1–102), PB1 (1–122), p62, and PB1-ZZ between 10 and 20 $e^-/Å^2$, respectively. Tomograms of negatively stained samples were acquired on a FEI Polara microscope using Serial EM software (Mastronarde, 2005) and by tilting the stage ±60° with a sampling step of 2° followed by smaller increments for higher angles using a Saxton acquisition scheme at a pixel size of 0.6 nm.

Image Processing

We performed single-particle based helical reconstruction of the PB1 domain samples using the previously described software package SPRING (Desfosses et al., 2014), which had been significantly modified from the original iterative helical real-space reconstruction procedure (Egelman, 2007). Processing details are summarized in Table S1. Helices were manually selected from the micrographs using the software E2HELIXBOXER from EMAN2 (Tang et al., 2007) and subsequently segmented using a step size of 70 Å and an image size of 500 Å. The stack of helical segments was convolved by the corresponding contrast-transfer functions (CTFs) determined from the micrographs using CTFFIND3 (Mindell and Grigorieff, 2003). Projection matching was performed as previously described (Sachse et al., 2007) by searching azimuthal angles and an out-of-plane tilt of ±12° including in-plane restraints derived from the segmentation procedure. To avoid over-fitting during iterative refinement, we successively low-pass filtered the 3D model reference after every iteration cycle. We chose the resolution filter cutoff at the 0.5 value of the square root of the FSC curve from the previous cycle such that it never exceeded 14 Å for PB1 (1–102) and PB1 (1–122) type T. This procedure is equivalent to independent half-set refinement (Scheres and Chen, 2012; Chen et al., 2013). Helical and dihedral symmetry were imposed by inserting symmetry-equivalent views into the 3D reconstruction. The resulting volume was corrected by dividing through an average 3D CTF squared volume including a Wiener filter constant of 2% of its maximum amplitude. Helical symmetry parameters of the PB1 (1–102), PB1 (1–122) type F and type T reconstructions were determined as

follows. First, we measured MPL using STEM. Second, we measured the visible helical pitch of PB1 (1–102), PB1 (1–122) type T and type F (Figures S1E, S1F, and S2A) from class averages that were obtained using k-means clustering of SX_KMEANS from SPARX (Hohn et al., 2007). Based on the molecular weight of the PB1 unit, we derived the helical rise of the helices and converted it to number of units per turn using the observed pitch. The parameters of PB1 (1–102), PB1 type T and type F were further refined around ±0.6 number of units per turn from the STEM-derived figures by optimizing the experimental versus the re-projected power spectrum of the 3D reconstruction (Desfosses et al., 2014). The class averages of PB1 type F (Figure S1B) possess an apolar appearance that suggested the presence of an additional dihedral symmetry. In order to confirm this hypothesis, we analyzed the structures of PB1 type F without imposed dihedral symmetry. To determine the relative orientation of the PB1 domain strands in these maps, we isolated the two PB1 strands from the EM density and superimposed them first in the same orientation using translation only and second in opposite orientation using translation and applying a 180° rotation with UCSF Chimera. This analysis favored the presence of antiparallel orientation of PB1 domains in the 3D reconstruction. The final symmetry agreement of all three 3D reconstructions was assessed by comparing the observed class averages with the re-projections and experimental with the simulated power spectrum in a side-by-side display. The resolution of all models was determined by Fourier shell correlation (FSC) of half data sets, giving an estimated resolution of 10.9 and 10.3 Å for the PB1 (1–102) and PB1 (1–122) type T (Figure S2F). The resolution of PB1 (1–122) type F could not be determined reliably due to weak signal for individual subunits in the raw images. Statistics of image processing for all three helical specimens are summarized in Table S1. Single-axis tomograms were processed and analyzed using IMOD (Kremer et al., 1996). Tilts were aligned using a fiducialless alignment option in Etomo and subregions of the final tomogram corresponding to individual helical filaments cropped out using in 3DMOD.

Atomic Model Building

The presented PB1 (1–102) and PB1 (1–122) type T maps were sharpened using a B-factor range from −800 to −1,100 1/Å^2 and low-pass filtered to the respective FSC 0.5 resolution cutoff. We built a homology model of PB1 (PDB code 2kkc >90% sequence identity) using the Swissmodel web server (http://swissmodel.expasy.org). Furthermore, in order to preserve the front-to-back interaction, we exchanged interface residues of the PB1 dimer (PDB code 2ktr) from the front and back side of molecule A and B to the monomeric homology model. To fit the PB1 model into the EM density, we expanded the homology PB1 model to a front-to-back tetramer using dimeric PB1 (PDB code 2ktr) as a template. We fitted the tetrameric PB1 strand manually into the PB1 reconstruction. Finally, we removed adjacent PB1 molecules and expanded it according to the final helical symmetry, which had been imposed on the 3D density.

Co-incubation, Co-sedimentation, Pelletation Assay, and EM Analysis

Purified p62 (0.8 and 1 μM) was co-incubated with LC3 (Novus Biologicals) at increasing molar ratios from 1:1 to 1:10 p62:His-LC3, and at decreasing molar ratios from 1:1 to 10:1 p62:His-LC3. Samples were kept on ice for 1 hr and spun at 150,000 × *g* for 1.5 hr at 4°C. After centrifugation supernatants were transferred to new tubes and pellets resuspended in an equal volume of buffer and applied on a 4%–12% SDS-PAGE gel. Proteins were visualized by Coomassie staining. To visualize LC3 at decreasing molar ratios, they were subjected to western blot analysis. Filamentous p62 samples were co-incubated with mono-, di-, and octa-ubiquitin (Boston Biochem) at molar ratio from 1:0.5 to 1:64, from 1:0.5 to 1:4, and from 1:0.5 to 1:4, respectively. Ubiquitin samples were analyzed by measuring p62 filaments from negatively stained EM images. Approximately 600 length measurements per sample were taken using ImageJ and the length distribution evaluated using histograms.

Cell Culture, Transfection, and Fluorescence Microscopy

HeLa cells were grown and transfected with siRNA-resistant mCherry-EYFP or GFP-p62 expression plasmid and siRNA (20 nM) against p62 as described (Pankiv et al., 2007), except that JetPRIME (Polyplus Transfection) was used for simultaneous transfection of plasmid DNA and siRNA. The R106E/R107E double mutation was introduced into GFP-p62 using the QuikChange site-directed mutagenesis kit (Stratagene) and verified by sequencing. RPE-1 cells were grown in DME-F12 medium with 10% fetal calf serum and transfected with an expression plasmid for myc-tagged ubiquitin using TransIT-LT1 (Mirus Bio LLC). Twenty-four hours after transfection cells were treated with 10 μg/ml puromycin for 2 hr before fixation and antibody staining using the 9E10 anti-Myc mouse monoclonal antibody and a guinea pig anti-p62 antibody (Progen). Knockdown efficiency was monitored by western blot (Figure S3). Confocal images were acquired on a Zeiss LSM510 Meta fluorescence microscope with identical settings for Alexa 488 (p62) and Alexa 555 (myc-Ub) and analyzed in Volocity v.6.2.1 (Perkin-Elmer). Cells were categorized as expressing high or low levels of myc-Ub, and non-transfected cells in the same well were used as controls.

ACCESSION NUMBERS

The EM densities of PB1 (1–102) and PB1 (1–122) type T filaments have been deposited at the EM databank (EMD-2936 and EMD-2937) and linked to the corresponding atomic assembly coordinates at the Protein Data Bank (entries 4uf8 and 4uf9).

SUPPLEMENTAL INFORMATION

Supplemental Information includes six figures and one table and can be found with this article online at http://dx.doi.org/10.1016/j.celrep.2015.03.062.

ACKNOWLEDGMENTS

We thank Olga Perisic and Roger Williams (MRC-LMB Cambridge, UK) for the kind gift of the p62 clone. We would like to express gratitude to Joseph Wall and Beth Lin (Brookhaven National Laboratory) for performing STEM analysis on our samples. We acknowledge support for the high-performance computing cluster from EMBL IT Services (Michael Wahlers). The technical assistance of Aud Øvervatn and the BioImaging Core Facility at the University of Tromsø with Kenneth Bowitz Larsen is greatly acknowledged. We thank Niko Grigorieff and Martin Beck for critically reading the manuscript. R.C. is grateful for receiving a predoctoral fellowship from Boehringer Ingelheim Fonds. The presented work was supported by a grant from the Fritz Thyssen Foundation (10.12.2.170).

Received: August 9, 2014
Revised: February 22, 2015
Accepted: March 24, 2015
Published: April 23, 2015

REFERENCES

Bjørkøy, G., Lamark, T., Brech, A., Outzen, H., Perander, M., Overvatn, A., Stenmark, H., and Johansen, T. (2005). p62/SQSTM1 forms protein aggregates degraded by autophagy and has a protective effect on huntingtin-induced cell death. J. Cell Biol. *171*, 603–614.

Chen, S., McMullan, G., Faruqi, A.R., Murshudov, G.N., Short, J.M., Scheres, S.H., and Henderson, R. (2013). High-resolution noise substitution to measure overfitting and validate resolution in 3D structure determination by single particle electron cryomicroscopy. Ultramicroscopy *135*, 24–35.

Christian, F., Krause, E., Houslay, M.D., and Baillie, G.S. (2014). PKA phosphorylation of p62/SQSTM1 regulates PB1 domain interaction partner binding. Biochim. Biophys. Acta *1843*, 2765–2774.

Ciani, B., Layfield, R., Cavey, J.R., Sheppard, P.W., and Searle, M.S. (2003). Structure of the ubiquitin-associated domain of p62 (SQSTM1) and implications for mutations that cause Paget's disease of bone. J. Biol. Chem. *278*, 37409–37412.

Desfosses, A., Ciuffa, R., Gutsche, I., and Sachse, C. (2014). SPRING - an image processing package for single-particle based helical reconstruction from electron cryomicrographs. J. Struct. Biol. *185*, 15–26.

Diaz-Avalos, R., King, C.Y., Wall, J., Simon, M., and Caspar, D.L. (2005). Strain-specific morphologies of yeast prion amyloid fibrils. Proc. Natl. Acad. Sci. USA *102*, 10165–10170.

Egelman, E.H. (2007). Single-particle reconstruction from EM images of helical filaments. Curr. Opin. Struct. Biol. *17*, 556–561.

Hohn, M., Tang, G., Goodyear, G., Baldwin, P.R., Huang, Z., Penczek, P.A., Yang, C., Glaeser, R.M., Adams, P.D., and Ludtke, S.J. (2007). SPARX, a new environment for Cryo-EM image processing. J. Struct. Biol. *157*, 47–55.

Ichimura, Y., Kumanomidou, T., Sou, Y.S., Mizushima, T., Ezaki, J., Ueno, T., Kominami, E., Yamane, T., Tanaka, K., and Komatsu, M. (2008). Structural basis for sorting mechanism of p62 in selective autophagy. J. Biol. Chem. *283*, 22847–22857.

Isogai, S., Morimoto, D., Arita, K., Unzai, S., Tenno, T., Hasegawa, J., Sou, Y.S., Komatsu, M., Tanaka, K., Shirakawa, M., and Tochio, H. (2011). Crystal structure of the ubiquitin-associated (UBA) domain of p62 and its interaction with ubiquitin. J. Biol. Chem. *286*, 31864–31874.

Itakura, E., and Mizushima, N. (2011). p62 Targeting to the autophagosome formation site requires self-oligomerization but not LC3 binding. J. Cell Biol. *192*, 17–27.

Jain, A., Lamark, T., Sjøttem, E., Larsen, K.B., Awuh, J.A., Øvervatn, A., McMahon, M., Hayes, J.D., and Johansen, T. (2010). p62/SQSTM1 is a target gene for transcription factor NRF2 and creates a positive feedback loop by inducing antioxidant response element-driven gene transcription. J. Biol. Chem. *285*, 22576–22591.

Johansen, T., and Lamark, T. (2011). Selective autophagy mediated by autophagic adapter proteins. Autophagy *7*, 279–296.

Kim, W., Bennett, E.J., Huttlin, E.L., Guo, A., Li, J., Possemato, A., Sowa, M.E., Rad, R., Rush, J., Comb, M.J., et al. (2011). Systematic and quantitative assessment of the ubiquitin-modified proteome. Mol. Cell *44*, 325–340.

Kishi-Itakura, C., Koyama-Honda, I., Itakura, E., and Mizushima, N. (2014). Ultrastructural analysis of autophagosome organization using mammalian autophagy-deficient cells. J. Cell Sci. *127*, 4089–4102.

Komatsu, M., Waguri, S., Koike, M., Sou, Y.S., Ueno, T., Hara, T., Mizushima, N., Iwata, J., Ezaki, J., Murata, S., et al. (2007). Homeostatic levels of p62 control cytoplasmic inclusion body formation in autophagy-deficient mice. Cell *131*, 1149–1163.

Komatsu, M., Kurokawa, H., Waguri, S., Taguchi, K., Kobayashi, A., Ichimura, Y., Sou, Y.S., Ueno, I., Sakamoto, A., Tong, K.I., et al. (2010). The selective autophagy substrate p62 activates the stress responsive transcription factor Nrf2 through inactivation of Keap1. Nat. Cell Biol. *12*, 213–223.

Kremer, J.R., Mastronarde, D.N., and McIntosh, J.R. (1996). Computer visualization of three-dimensional image data using IMOD. J. Struct. Biol. *116*, 71–76.

Kuusisto, E., Salminen, A., and Alafuzoff, I. (2001). Ubiquitin-binding protein p62 is present in neuronal and glial inclusions in human tauopathies and synucleinopathies. Neuroreport *12*, 2085–2090.

Lamark, T., Perander, M., Outzen, H., Kristiansen, K., Øvervatn, A., Michaelsen, E., Bjørkøy, G., and Johansen, T. (2003). Interaction codes within the family of mammalian Phox and Bem1p domain-containing proteins. J. Biol. Chem. *278*, 34568–34581.

Lau, A., Wang, X.J., Zhao, F., Villeneuve, N.F., Wu, T., Jiang, T., Sun, Z., White, E., and Zhang, D.D. (2010). A noncanonical mechanism of Nrf2 activation by autophagy deficiency: direct interaction between Keap1 and p62. Mol. Cell. Biol. *30*, 3275–3285.

Leach, R.J., Singer, F.R., Ench, Y., Wisdom, J.H., Pina, D.S., and Johnson-Pais, T.L. (2006). Clinical and cellular phenotypes associated with sequestosome 1 (SQSTM1) mutations. J. Bone Miner. Res. *21* (*2*), 45–50.

Long, J., Garner, T.P., Pandya, M.J., Craven, C.J., Chen, P., Shaw, B., Williamson, M.P., Layfield, R., and Searle, M.S. (2010). Dimerisation of the UBA domain of p62 inhibits ubiquitin binding and regulates NF-kappaB signalling. J. Mol. Biol. *396*, 178–194.

Mastronarde, D.N. (2005). Automated electron microscope tomography using robust prediction of specimen movements. J. Struct. Biol. *152*, 36–51.

Matsumoto, G., Wada, K., Okuno, M., Kurosawa, M., and Nukina, N. (2011). Serine 403 phosphorylation of p62/SQSTM1 regulates selective autophagic clearance of ubiquitinated proteins. Mol. Cell *44*, 279–289.

Mindell, J.A., and Grigorieff, N. (2003). Accurate determination of local defocus and specimen tilt in electron microscopy. J. Struct. Biol. *142*, 334–347.

Mizushima, N., Yoshimori, T., and Ohsumi, Y. (2011). The role of Atg proteins in autophagosome formation. Annu. Rev. Cell Dev. Biol. *27*, 107–132.

Morimoto, D., Walinda, E., Fukada, H., Sou, Y.S., Kageyama, S., Hoshino, M., Fujii, T., Tsuchiya, H., Saeki, Y., Arita, K., et al. (2015). The unexpected role of polyubiquitin chains in the formation of fibrillar aggregates. Nat. Commun. *6*, 6116.

Moscat, J., and Diaz-Meco, M.T. (2009). p62 at the crossroads of autophagy, apoptosis, and cancer. Cell *137*, 1001–1004.

Moscat, J., and Diaz-Meco, M.T. (2012). p62: a versatile multitasker takes on cancer. Trends Biochem. Sci. *37*, 230–236.

Paine, M.G., Babu, J.R., Seibenhener, M.L., and Wooten, M.W. (2005). Evidence for p62 aggregate formation: role in cell survival. FEBS Lett. *579*, 5029–5034.

Pankiv, S., Clausen, T.H., Lamark, T., Brech, A., Bruun, J.A., Outzen, H., Øvervatn, A., Bjørkøy, G., and Johansen, T. (2007). p62/SQSTM1 binds directly to Atg8/LC3 to facilitate degradation of ubiquitinated protein aggregates by autophagy. J. Biol. Chem. *282*, 24131–24145.

Ramesh Babu, J., Lamar Seibenhener, M., Peng, J., Strom, A.L., Kemppainen, R., Cox, N., Zhu, H., Wooten, M.C., Diaz-Meco, M.T., Moscat, J., and Wooten, M.W. (2008). Genetic inactivation of p62 leads to accumulation of hyperphosphorylated tau and neurodegeneration. J. Neurochem. *106*, 107–120.

Sachse, C., Chen, J.Z., Coureux, P.D., Stroupe, M.E., Fändrich, M., and Grigorieff, N. (2007). High-resolution electron microscopy of helical specimens: a fresh look at tobacco mosaic virus. J. Mol. Biol. *371*, 812–835.

Saio, T., Yokochi, M., and Inagaki, F. (2009). The NMR structure of the p62 PB1 domain, a key protein in autophagy and NF-kappaB signaling pathway. J. Biomol. NMR *45*, 335–341.

Saio, T., Yokochi, M., Kumeta, H., and Inagaki, F. (2010). PCS-based structure determination of protein-protein complexes. J. Biomol. NMR *46*, 271–280.

Sawa-Makarska, J., Abert, C., Romanov, J., Zens, B., Ibiricu, I., and Martens, S. (2014). Cargo binding to Atg19 unmasks additional Atg8 binding sites to mediate membrane-cargo apposition during selective autophagy. Nat. Cell Biol. *16*, 425–433.

Scheres, S.H.W., and Chen, S. (2012). Prevention of overfitting in cryo-EM structure determination. Nat. Methods *9*, 853–854.

Stumptner, C., Fuchsbichler, A., Zatloukal, K., and Denk, H. (2007). In vitro production of Mallory bodies and intracellular hyaline bodies: the central role of sequestosome 1/p62. Hepatology *46*, 851–860.

Tang, G., Peng, L., Baldwin, P.R., Mann, D.S., Jiang, W., Rees, I., and Ludtke, S.J. (2007). EMAN2: an extensible image processing suite for electron microscopy. J. Struct. Biol. *157*, 38–46.

Wall, J.S., and Simon, M.N. (2001). Scanning transmission electron microscopy of DNA-protein complexes. Methods Mol. Biol. *148*, 589–601.

Wilson, M.I., Gill, D.J., Perisic, O., Quinn, M.T., and Williams, R.L. (2003). PB1 domain-mediated heterodimerization in NADPH oxidase and signaling complexes of atypical protein kinase C with Par6 and p62. Mol. Cell *12*, 39–50.

Zatloukal, K., Stumptner, C., Fuchsbichler, A., Heid, H., Schnoelzer, M., Kenner, L., Kleinert, R., Prinz, M., Aguzzi, A., and Denk, H. (2002). p62 Is a common component of cytoplasmic inclusions in protein aggregation diseases. Am. J. Pathol. *160*, 255–263.

Zhang, Y., Wang, W., Chen, J., Zhang, K., Gao, F., Gao, B., Zhang, S., Dong, M., Besenbacher, F., Gong, W., et al. (2013). Structural insights into the intrinsic self-assembly of Par-3 N-terminal domain. Structure *21*, 997–1006.